Geoscientific
Model Development
Discussions

Open Access

Non-orthogonal version of the arbitrary polygonal C-grid and a new diamond grid

H. Weller

Meteorology, University of Reading, Reading, UK

Correspondence to: H. Weller (h.weller@reading.ac.uk)

GMDD

6, 6035–6074, 2013

Diamond C-grid

H. Weller

Title Page

Abstract	Introduction
Conclusions	References
Tables	Figures

◀ | ▶

◀ | ▶

Back | Close

Full Screen / Esc

Printer-friendly Version

Interactive Discussion

Abstract

Quasi-uniform grids of the sphere have become popular recently since they avoid parallel scaling bottlenecks associated with the poles of latitude-longitude grids. However quasi-uniform grids of the sphere are often non-orthogonal. A version of the C-grid for arbitrary non-orthogonal grids is presented which gives some of the mimetic properties of the orthogonal C-grid. Exact energy conservation is sacrificed for improved accuracy and the resulting scheme numerically conserves energy and potential enstrophy well. The non-orthogonal nature means that the scheme can be used on a cubed sphere. The advantage of the cubed sphere is that it does not admit the computational modes of the hexagonal or triangular C-grids. On various shallow-water test cases the non-orthogonal scheme on a cubed sphere has accuracy less than or equal to the orthogonal scheme on an orthogonal hexagonal icosahedron.

   A new diamond grid is presented consisting of quasi-uniform quadrilaterals which is more orthogonal than the equal-angle cubed sphere but with otherwise similar properties. It performs better than the cubed sphere in every way and should be used instead in codes which allow a flexible grid structure.

1   Introduction

Quasi-uniform grids of the sphere have become popular recently since they avoid parallel scaling bottlenecks associated with the poles of latitude-longitude grids. The predominant groups of quasi-uniform grid are hexagonal icosahedral, triangular icosahedral and cubed-sphere (Weller et al., 2009). There is also an octagonal grid (Rančić et al., 2008) that has not been used much but has similar properties to the cubed sphere and there are reduced or skipped lat-lon grids which are not much used except in conjunction with spectral transform models (Hortal and Simmons, 1991; White, 2003). The details of the grid are critically important for low-order finite volume methods

that rely on super-convergence for accuracy (second order accuracy only for a sufficiently smooth grid).

The C-grid discretisation was extended to hexagons (Thuburn, 2008) and then to orthogonal polygons (TRiSK, Thuburn et al., 2009; Ringler et al., 2010) to facilitate its use on quasi-uniform grids of the sphere. TRiSK has mostly been used on Voronoi tesselations of the sphere (e.g. Ringler et al., 2008) which are orthogonal (the primal and dual edges cross at right angles) and each shape has more than (or occasionally equal to) four sides. C-grids based on primal cells with more than four sides in 2-D will have more than twice as many velocity degrees of freedom (dofs) as mass dofs and will therefore suffer from spurious computational modes (Staniforth and Thuburn, 2012). The hexagonal C-grid suffers from a branch of spurious Rossby modes Thuburn (2008) which do not interact correctly with the mass. The triangular C-grid does not have enough velocity dofs and so suffers from spurious divergent modes (Danilov, 2010; Gassmann, 2011). The spurious modes on triangles can be controlled by strong diffusion (Gassmann, 2011) or strong hyper-diffusion (Wan et al., 2013). The spurious modes on hexagons can be controlled using upwinded advection of potential vorticity (e.g. Weller, 2012) which does not destroy energy. However a more efficient discretisation would have the correct ratio of dofs and would not need to control spurious behaviour in the excess dofs. The correct ratio of dofs is achieved by using grids of quadrilaterals, such as the cubed-sphere grid. However grids of the sphere using quadrilaterals are either non-orthogonal (e.g. the equal-angle cubed sphere, Fournier et al., 2004), have large variations of cell size (e.g. the conformal cubed sphere, Rančić et al., 1996) or are locally inhomogeneous (such as kite grids, Weller et al., 2012). This provides motivation for more orthogonal quadrilateral grids of the sphere and a C-grid discretisation that works on non-orthogonal grids.

Thuburn and Cotter (2012) describe some desirable mimetic properties of atmospheric models (mimicking the properties of the continuous equations). Their mimetic properties are 1–6. Property 7 is clearly also desirable:

1. C-grid staggering (assuming a finite difference or finite volume approach) for accurate dispersion of intertio-gravity waves.

2. Mass conservation.

3. Curl-free pressure gradient.

4. Energy conserving pressure terms.

5. Energy conserving Coriolis term.

6. Steady geostrophic modes.

7. Second-order accuracy (or higher).

The TRiSK scheme (Thuburn et al., 2009; Ringler et al., 2010) gives properties (1–6) on orthogonal polygonal grids but it will be demonstrated that the discretisation of the perpendicular (perp) operator (for calculating tangential velocities from neighbouring normal velocities at edges) is inconsistent (i.e. zeroth order accurate) even on the smoothest hexagonal icosahedral grids of the sphere. Extending TRiSK to non-orthogonal grids may ameliorate the lack of convergence of TRiSK since points other than the Voronoi generating points can be used as the cell centre in order to optimise aspects of the grid to improve accuracy of the perp operator.

Thuburn and Cotter (2012) set out the mathematical constraints for mimetic C-grid discretisations on non-orthogonal grids but did not give an example of such a scheme. Subsequently, Thuburn et al. (2013) proposed a scheme suitable for grids whose duals consist of only triangles and quadrilaterals. However the results on cubed-sphere grids were much less accurate than those using similar resolution hexagonal-icosahedra. A variety of mixed finite-element schemes for grids of triangles or quadrilaterals have been proposed which give the above properties and second-order accuracy by constructing and inverting global mass matrices at every time-step (Cotter and Shipton, 2012; Cotter and Thuburn, 2013).

A new diamond grid of quadrilaterals is introduced in Sect. 2 which is more orthogonal than the equal-angle cubed sphere and nearly as uniform. The properties of the diamond grid are compared with those of the cubed sphere and orthogonal and non-orthogonal versions of the hexagonal icosahedron. In Sect. 3, a more accurate non-orthogonal version of TRiSK is proposed that forgoes energy conservation for better accuracy than the scheme of Thuburn et al. (2013). The accuracy of the perp operator is explored in Sect. 5 and the results of shallow-water test cases are presented in Sect. 6.

2   Quasi-uniform grids of the sphere

Four types of grid are considered; the Heikes and Randall (1995) optimised version of the hexagonal-icosahedron, a non-orthogonal version of the same with the dual vertices moved from the Voronoi generating points to the centroids of the polygons, the equal angle cubed sphere and a diamondised version of the cubed sphere (Fig. 1). The diamond grid is constructed by replacing each edge of the cubed sphere with a primal cell whose vertices consist of the two vertices of the original edge and the cell centres either side of the edge (bottom right of Fig. 1). This is topologically different from the cubed sphere and different from the dual of the cubed sphere although it still suffers from the problem of having 3 squares meet at one vertex at 8 locations in the grid. The panels of the cubed sphere and diamond grids are shown in Fig. 2.

The skewness and non-orthogonality of coarse versions of these grids are shown in Fig. 1. The non-orthogonality is the difference between the angle between the primal and dual edges (in degrees) and 90°. The non-orthogonality is shown from black (orthogonal) to blue (non-orthogonal) on the primal grid edges. The skewness of edge e, s_e, measures the departure from the edge centre of the primal-dual edge cross-over point:

$$s_e = \frac{\text{dist}\left(\boldsymbol{x}_e, \frac{1}{2}(\boldsymbol{x}_v + \boldsymbol{x}_w)\right)}{\text{dist}(\boldsymbol{x}_v, \boldsymbol{x}_w)} \qquad (1)$$

where $\boldsymbol{x}_v$ and $\boldsymbol{x}_w$ are the primal vertices at either end of edge e. The distance between the edge centre and the edge cross-over point (the numerator of the skewness) is marked with an s in the top right panel of Fig. 1. The skewness of the primal and dual meshes is different but the skewness of the primal mesh is shown from red (no skewness) to yellow on the dual edges. In Fig. 1, the diamond grid is more orthogonal and less skew than the cubed sphere, a result that holds at all resolutions considered.

The Heikes and Randall (1995) (HR) grid (top left of Fig. 1) is orthogonal and optimised to minimise skewness. This minimises the error of discretising a Laplacian but the value at the dual vertex is not a second-order approximation of the primal cell average because the dual vertex is not at the centroid. In moving the dual vertex to the centroid of the primal cell (top right of Fig. 1), the grid becomes centroidal but non-orthogonal and also the skewness is increased. An alternative is the centroidal Voronoi grid (Ringler et al., 2008) which is orthogonal but more skew than the HR grid. Using non-orthogonal grids opens up many more options for optimising a combination of the orthogonality, skewness, uniformity and centroidality of both the primal and dual grids. However this has not been done.

Some of the properties of the grids at different resolutions are shown in Table 1. The non-centroidality is defined as the distance between the dual vertex and the cell centroid of a primal cell divided by the square root of the primal call area:

$$\text{non-centroidality} = \frac{\text{dist}(\boldsymbol{x}_i, \text{centroid}(i))}{\sqrt{A_i}}. \qquad (2)$$

By making the primal centroidal, the dual may become less centroidal but we have not considered optimising both. The non-orthogonal HR grid has non-orthogonality of less than 1° and skewness similar to the orthogonal version.

Full Screen / Esc

Printer-friendly Version

Interactive Discussion

The equal-angle cubed-sphere grid has non-orthogonality increasing with resolution up to 30° for the resolutions considered and maximum skewness of 0.17 at the corners. The cubed sphere that we have chosen is non-centroidal with a centroidal dual.

The diamondised cubed sphere is more orthogonal than the cubed sphere in the mean and maximum (less that 10°). The skewness and non-centroidality are similar. The diamond grid was constructed to have a centroidal primal but a non-centroidal dual. The diamond grid is slightly less uniform that the cubed sphere ($\frac{\Delta x_{max}}{\Delta x_{min}} < 2.03$ for the diamond grid whereas $\frac{\Delta x_{max}}{\Delta x_{min}} < 1.8$ for the cubed sphere) but otherwise does not appear to suffer from any deficiencies relative to the cubed sphere.

The impacts of the different grid structures on the accuracy of the perp operator will be seen in Sect. 5 and on the solution of the shallow-water equations in Sect. 6.

3   The non-orthogonal C-grid discretisation

We present a discretisation of the rotating, non-linear shallow-water equations in vector-invariant form in which the continuity and momentum equations are:

$$\frac{\partial \phi}{\partial t} + \nabla \cdot (\phi \boldsymbol{v}) = 0 \tag{3}$$

$$\frac{\partial \boldsymbol{v}}{\partial t} + \zeta \boldsymbol{v}^{\perp} + \nabla \left(\phi + \frac{|\boldsymbol{v}|^2}{2} \right) = \boldsymbol{0} \tag{4}$$

where ϕ is the geopotential (fluid depth times gravity), $\boldsymbol{v}$ is the horizontal velocity, $\boldsymbol{v}^{\perp} = \boldsymbol{k} \times \boldsymbol{v}$ where $\boldsymbol{k}$ is the local unit vertical vector, $\zeta = f + \xi$ is the absolute vorticity, where $f = 2\boldsymbol{k} \cdot \boldsymbol{\Omega}$ is the Coriolis parameter associated with rotation $\boldsymbol{\Omega}$ and $\xi = \boldsymbol{k} \cdot (\nabla \times \boldsymbol{v})$ is the relative vorticity.

3.1 Notation

The notation has some minor differences from Thuburn and Cotter (2012). The primal (solid) and dual (dashed) grids from Thuburn and Cotter (2012) are shown in Fig. 3 with the surface normal vectors, lengths and fluxes. Edge e of the primal grid has length $p = |\boldsymbol{p}|$, normal vector $\boldsymbol{p}$ and tangential vector $\boldsymbol{p}^\perp$. Edge e of the dual grid has normal vector $\boldsymbol{d}$ and tangential vector $\boldsymbol{d}^\perp$. Here we restrict our attention to a low-order finite volume discretisation so that the volume (or area) flux across edge e is $U_e = \boldsymbol{v}_e \cdot \boldsymbol{p}$ and the circulation along dual edge e is $V_e = \boldsymbol{v} \cdot \boldsymbol{d}^\perp$. Lower case variable names indicate values sampled at a point whereas upper case names are integrated values. Primal cells are indexed or denoted by i or j and dual cells are indexed or denoted by v or w. These definitions and some of the finite volume approximations are given in Table 2.

3.2 Discretised momentum and continuity equations

The prognostic variables of the shallow-water equations of a C-grid are usually cell average geopotential, ϕ_i, and the normal component of the velocity at the cell edges, $u_e = \boldsymbol{v} \cdot \hat{\boldsymbol{p}}_e$. However on the non-orthogonal C-grid, the prognostic velocity variable is V_e (Thuburn and Cotter, 2012). We consider split space-time discretisation and so the discretisation of the temporal derivatives is considered separately. The spatially discretised continuity equation for ϕ_i and momentum equation for V_e can be written:

$$\frac{\partial \phi_i}{\partial t} + \nabla \cdot H\left(\phi_e V_e\right) = 0 \tag{5}$$

$$\frac{\partial V_e}{\partial t} + \frac{1}{2}\left(q_e\left(\phi_e U_e\right)^\perp + \left(q_e \phi_e U_e\right)^\perp\right) + \nabla_\mathrm{d}\left(\phi + k\right) = 0. \tag{6}$$

The discretisation of each of the terms will now be described, including the H operator and the graident along a dual edge, ∇_d.

3.2.1 Perp operator, $\perp$

The perp operator, $\perp$, in Eq. (6) is the discrete operator described in Thuburn et al. (2009) for mapping from fluxes on the primal grid to fluxes on the dual grid. This operator ensures that the divergence of the mapped fluxes is a convex combination of the divergence of the fluxes on the primal grid. This is why the discrete perp operator acts on the flux, U_e, (in the $\boldsymbol{p}$ direction) and maps to the $\boldsymbol{d}$ direction, despite $\boldsymbol{p}$ and $\boldsymbol{d}$ not being at right angles. This operator is inconsistent (zeroth order accurate) even on an orthogonal grid but does not always prevent convergence with resolution of the shallow-water equations (see Sects. 5 and 6). The perp operator is defined to be:

$$U_e^\perp = \sum_{e' \in EC(i), EC(j)} w_{ee'} U_{e'} \tag{7}$$

where primal cells i and j are the cells either side of edge e_{p}, $EC(i)$ means the edges of cell i and Thuburn et al. (2009) derived the weights $w_{ee'}$:

$$w_{ee'} = \pm \left(\frac{1}{2} - \sum_v \frac{A_{iv}}{A_i} \right) \tag{8}$$

where the vs are the vertices in a walk between edges e and e'. If the walk starts in the $\boldsymbol{p}^\perp$ direction and if $n_{ei} = 1$ then the sign is positive.

3.2.2 Mapping from primal cell averages to edges

In order to ensure energetic consistency, the mapping of ϕ from cells to edges ($\phi_i \to \phi_e$) must use the same weighting as will be used to calculating the kinetic energy (Eq. 10):

$$\phi_e = \frac{A_{ie}}{A_e} \phi_i + \frac{A_{je}}{A_e} \phi_j \tag{9}$$

where cells i and j are either side of edge e. This is the reverse of linear interpolation and ensures an exact transfer between kinetic and potential energy. However, higher-order upwind interpolations can be used instead, foregoing this form of energy conservation in favour of a smoother geopotential field. Here, we will present results using CLUST (Weller, 2012) with a blending of 50 % between linear and linear-upwind differencing which gives smoother advection of geopotential (see Sect. 3.2.4).

3.2.3 PV and curl on dual cells

From Ringler et al. (2010), q_v is discretised as:

$$q_v = \frac{f_v + \text{curl}\,(V_e)_v}{\phi_v}$$

where $\phi_v = \sum_{i \in CV(v)} A_{iv}\phi_i$ is the conservative mapping of ϕ from the primal to the dual grid and, from Thuburn and Cotter (2012), the curl is discretised as:

$$\text{curl}\,(V_e)_v = \frac{1}{A_v} \sum_{e \in EC(v)} n_{ev} V_e.$$

3.2.4 Mapping pv from dual cells to edges

The potential vorticity at the edge, q_e, is interpreted as the pv at the primal and dual edges. It is interpolated from surrounding q_v values from an upwind-biased stencil using CLUST which was developed for mapping pv from vertices to edges of the polygonal C-grid Weller (2012). The CLUST blending coefficient between linear differencing and linear upwind used is 0.5. It is essential to use CLUST for this work rather than a conventional high-order upwind or monotonic advection scheme such as quadratic-upwind, linear-upwind or a TVD scheme such as van Leer. The conventional schemes have switching between upwind on either side of an edge when the flow is aligned with

the edge. When used for interpolating pv on the dual of the C-grid, this leads to errors. The advantage of CLUST is that it blends smoothly with linear when the flow is aligned with the edge so there is no switching. APVM (Ringler et al., 2010, which is equivalent to Lax–Wendroff) could also be used as it does not involve switching but CLUST was found to control the grid-scale pv noise better (Weller, 2012).

3.2.5 Energy conserving coriolis flux averaging

The averaging between $q_e (\phi_e U_e)^\perp$ and $(q_e \phi_e U_e)^\perp$ in Eq. (6) is necessary for the Coriolis force to be energetically neutral (Ringler et al., 2010). Without this averaging (if this term is simply represented as $q_e (\phi_e U_e)^\perp$) the pv evolves exactly as if it were advected by the fluxes $U_e^\perp$ by the advection scheme used to map pv from dual cells to edges. Thus high order, monotonic advection of pv can be obtained. However, numerical tests by Ringler et al. (2010) and further unpublished work have found the energy conserving version to generate more accurate solutions without serious oscillations in pv. However the non-energy conserving version is used by Thuburn et al. (2013).

3.2.6 Gradients along dual edges

The gradient of ϕ along dual edge e, integrated along the edge, between cells i and j is:

$$\nabla_d \phi = d \frac{n_{ei} (\phi_j - \phi_i)}{d} = n_{ei} (\phi_j - \phi_i).$$

This gradient is also used for the kinetic energy.

3.2.7 Kinetic energy

The kinetic energy in primal cell i is defined as:

$$k_i = \frac{1}{2A_i} \sum_{e \in EC(i)} \frac{\text{dist}(\boldsymbol{x}_e, \boldsymbol{x}_i)}{d} U_e V_e = \frac{1}{2A_i} \sum_{e \in EC(i)} \frac{A_{ie}}{A_e} U_e V_e \tag{10}$$

where $\text{dist}(\boldsymbol{x}_e, \boldsymbol{x}_i)$ is defined in Sect. 3.2.13. Ringler et al. (2010) weighted the edge
contributions by $\frac{1}{2}$ rather than A_{ie}/A_e. Then, in order to achieve energetic consistency,
they use $A_i = 1/4 \sum_e A_e$ which gives the correct area on Voronoi grids for which the
edges bisect the lines between the Voronoi generating points. Weller et al. (2012) suggest the weighting as in Eq. (10) for non-Voronoi grids. For energetic consistency, the
same weighting must be used for mapping the geopotential from cells to edges (see
Sect. 3.2.2).

3.2.8 Divergence operator

The divergence of a vector $\boldsymbol{v}_e$ defined at edges in cell i is given by Gauss's divergence
theorem:

$$(\nabla \cdot \boldsymbol{v})_i = \frac{1}{A_i} \sum_{e \in EC(i)} n_{ei} \boldsymbol{v}_e \cdot \boldsymbol{p} = \frac{1}{A_i} \sum_{e \in EC(i)} n_{ei} U_e. \tag{11}$$

Thuburn and Cotter (2012) suggest operator H to transform V_e into U_e so that:

$$(\nabla \cdot (\phi \boldsymbol{v}))_i = \frac{1}{A_i} \sum_{e \in EC(i)} n_{ei} \phi_e U_e = \frac{1}{A_i} \sum_{e \in EC(i)} n_{ei} H(\phi_e V_e). \tag{12}$$

The H operator is described further in Sect. 3.2.9 below.

3.2.9 *H* operator

The *H* operator transforms from the set of *V* values to the *U* values and is therefore referred to as a non-orthogonal correction.

3.2.10 Symmetric *H*

Thuburn and Cotter (2012) proved that energetic consistency is achieved if *H* is symmetric and positive definite but they did not suggest the form of *H* for non-orthogonal grids. Thuburn et al. (2013) suggest an *H* operator with the desired properties for grids whose dual consists of quadrilaterals or triangles:

$$U_e = H(V_e) = \sum_{e'(\neq e)} \frac{1}{f_{e'}} \frac{\left(V_e \boldsymbol{d}_{e'}^{\perp} - V_{e'} \boldsymbol{d}_e^{\perp}\right) \cdot \boldsymbol{d}_{e'}^{\perp}}{|\boldsymbol{d}_e^{\perp} \times \boldsymbol{d}_{e'}^{\perp}|} \tag{13}$$

where the stencil of edges e' consists of the edges of the dual sharing one vertex with e and $f_e = 4$ when dual edges e and e' are edges of the same quadrilateral and $f_e = 6$ when e and e' are edges of the same triangle. All Voronoi grids and many other grids of polygons have dual grids consisting of only triangles and the dual of the cubed sphere grid consists of quadrilaterals and 8 triangles. So this operator should cover most of the grids anyone would be interested in. It is also first order accurate provided that the primal grid vertices are located at the barycentres of the surrounding cells. However, in general, the off-diagonal terms of *H* do not vanish as the grids tends towards an orthogonal grid. The accuracy of solutions using this operator will be presented in Sect. 6.

3.2.11 Asymmetric *H*

It would seem logical to have an *H* operator with vanishing off-diagonal terms as the grid becomes orthogonal. The first/second order operator for reconstructing cell centre

Back | Close

Full Screen / Esc

Printer-friendly Version

Interactive Discussion

vectors from normal components at edges in OpenFOAM (2013) is:

$$\boldsymbol{v}_i = T_i^{-1} \sum_{e \in \text{EC}(i)} \widehat{\boldsymbol{p}}_e U_e \tag{14}$$

where $T_i = \sum_{e \in \text{EC}(i)} \widehat{\boldsymbol{p}}_e \boldsymbol{p}_e$. T_i is a 3×3 tensor so not computationally expensive to invert and is only dependent on geometry and so can be pre-computed. It can be shown that this operator will exactly reconstruct a uniform velocity field and for non-uniform velocities, it is a least-squares fit. Alternatively, to reconstruct dual cell velocity, $\boldsymbol{v}_v$ from V_e we can use:

$$\boldsymbol{v}_v = T_v^{-1} \sum_{e \in \text{EC}(v)} \widehat{\boldsymbol{d}}_e^{\perp} V_e \tag{15}$$

where $T_v = \sum_{e \in \text{EC}(v)} \widehat{\boldsymbol{d}}_e^{\perp} \boldsymbol{d}_e^{\perp}$. We can then interpolate the $\boldsymbol{v}_v$s from the dual cells to the dual edges using any centred or upwind-biased interpolation. We will show results in Sect. 6 using mid-point interpolation. The resulting velocity on edges is referred to as $\boldsymbol{v}_e'$, with the prime because this is not the final velocity that will give us U_e. We require $U_e = p_e/d_e V_e$ for an orthogonal grid ($\widehat{\boldsymbol{p}} = \widehat{\boldsymbol{d}}^{\perp}$) so we can correct $\boldsymbol{v}_e'$ to give exactly V_e in the direction $\widehat{\boldsymbol{d}}_e^{\perp}$:

$$\boldsymbol{v}_e = \frac{V_e}{d_e} \widehat{\boldsymbol{d}}_e^{\perp} + \boldsymbol{v}_e' - \left(\boldsymbol{v}_e' \cdot \widehat{\boldsymbol{d}}_e^{\perp} \right) \widehat{\boldsymbol{d}}_e^{\perp} \tag{16}$$

from which we can write down $U_e = H(V_e)$:

$$U_e = \boldsymbol{v}_e \cdot \boldsymbol{p}_e \tag{17}$$

$$= \frac{\widehat{\boldsymbol{d}}_e^{\perp}}{d_e} \cdot \boldsymbol{p}_e V_e + \boldsymbol{v}_e' \cdot \left(\boldsymbol{p}_e - \widehat{\boldsymbol{d}}_e^{\perp} \left(\widehat{\boldsymbol{d}}_e^{\perp} \cdot \boldsymbol{p}_e \right) \right). \tag{18}$$

For nearly orthogonal grids this operator is close to diagonal so the requirement for positive definiteness should easily be met for most grids. However this operator is not symmetric. In fact the requirement for symmetry is not consistent with the requirement that $H_{ee'} = 0$ for all $e \neq e'$ if $\widehat{\boldsymbol{p}}_e \cdot \widehat{\boldsymbol{d}}_e^{\perp} = 1$, since if we also have $\widehat{\boldsymbol{p}}_{e'} \cdot \widehat{\boldsymbol{d}}_{e'}^{\perp} \neq 1$ the we may have $H_{e'e} \neq 0$.

The relative merits and accuracy of the symmetric and asymmetric H will be assessed in Sect. 6.

3.2.12 Full velocity field at cell edges

The full velocity field at cell edges is needed in CLUST and for post-processing such as calculating errors and error metrics. Due to the inconsistency of the perp operator, Eq. (16) is used to reconstruct the full velocity field.

3.2.13 Spherical areas and distances

All distances (or lengths) are great circle distances so that the distance between points $\boldsymbol{x}_v$ and $\boldsymbol{x}_w$ is:

$$\text{dist}(\boldsymbol{x}_v, \boldsymbol{x}_w) = 2a \sin^{-1} \frac{1}{2} |\boldsymbol{x}_v - \boldsymbol{x}_w| \qquad (19)$$

where a is the magnitude of both $\boldsymbol{x}_v$ and $\boldsymbol{x}_w$. The areas on the surface of the sphere are calculated to be consistent with the distances to retain the correct mimetic properties. Thus the area of a triangle with points $\boldsymbol{x}$, $\boldsymbol{y}$ and $\boldsymbol{z}$ on a sphere of radius a is:

$$a^2/2 \, \text{dist}(\boldsymbol{y}, \boldsymbol{x})\text{dist}(\boldsymbol{z}, \boldsymbol{x})|(\widehat{\boldsymbol{z} - \boldsymbol{x}}) \times (\widehat{\boldsymbol{y} - \boldsymbol{x}})|. \qquad (20)$$

Areas A_{ie}, A_{iv}, A_i and A_v are composed of the sums of triangles A_{ive}, as shown in Fig. 3.

3.2.14 Semi-implicit solution technique

The momentum and continuity equations are solved semi-implicitly using Crank–Nicolson for the implicit terms. Two outer iterations are used so that, for the first iteration the explicit terms are solved with Euler-explicit and the second iteration uses 50–50 weighting of the old and new values so that the explicit terms are second order, with the same weighting as the implicit terms. For the simplest possible implementation, H is split into diagonal and off diagonal elements: $H = H_d + H_{off}$ and only the diagonal terms are included in the implicit part. The off diagonal terms are lagged corrections. Between times-levels n and $n + 1$ this gives:

$$\frac{\phi_i^{n+1} - \phi_i^n}{\Delta t} + \frac{1}{2}\nabla \cdot H\left(\phi_e^n V_e^n\right) + \frac{1}{2}\nabla \cdot H_d\left(\phi_e^\ell V_e^{n+1}\right) + \frac{1}{2}\nabla \cdot H_{off}\left(\phi_e^\ell V_e^\ell\right) = 0 \tag{21}$$

$$\frac{V_e^{n+1} - V_e^n}{\Delta t} + \frac{1}{4}\left(q_e\left(\phi_e^n U_e^n\right)^\perp + \left(q_e^n \phi_e^n U_e^n\right)^\perp\right) + \frac{1}{2}\nabla_d\left(\phi^n + k^n\right)$$

$$+ \frac{1}{4}\left(q_e^\ell\left(\phi_e^\ell U_e^\ell\right)^\perp + \left(q_e^\ell \phi_e^\ell U_e^\ell\right)^\perp\right) + \frac{1}{2}\nabla_d\left(\phi^{n+1} + k^\ell\right) = \mathbf{0}. \tag{22}$$

where values at time level ℓ are at time-level n for the first iteration and they are the most up to date value (but not implicit) for the second iteration. Using just two iterations, the explicit scheme is the Heun scheme which is weakly unstable. However the instability is not seen in the simulations undertaken. An additional explicit step would remove the instability if needed. Equations (21) and (22) are solved simultaneously for ϕ^{n+1} by substituting V^{n+1} from Eq. (22) into Eq. (21) (taking the Schur complement) to form a Helmholtz equation which is solved using a conjugate gradient solver with incomplete Cholesky pre-conditioning (OpenFOAM, 2013).

4 Linear stability

The normal modes (eigen values) of the model for the linearised shallow water equations

$$\frac{\partial \boldsymbol{u}}{\partial t} + f \boldsymbol{u}^\perp = -g \nabla h, \qquad \frac{\partial h}{\partial t} + H \nabla \cdot \boldsymbol{u} = 0$$

5   are found using the method of Weller et al. (2012) using $f = 2\boldsymbol{k} \cdot \boldsymbol{\Omega}$, $\boldsymbol{\Omega} = (0, 0, 7.292 \times 10^{-5})\,\mathrm{s}^{-1}$, $H = 1000\,\mathrm{m}$ and $g = 9.80616\,\mathrm{m\,s}^{-2}$. The corresponding eigen vectors give us the amplification factor amplitude and frequencies of the normal modes and are shown in Fig. 4 for the cubed sphere grid with 6 × 6 cells per panel (648 dofs) using the symmetric and asymmetric H operators. Crank–Nicolson time-stepping with a time-step of

10   1 s is used with the Coriolis term treated explicitly and updated 4 times per time-step to ensure stability. The symmetric H ensures that the scheme is energy conserving and so the amplitude (the magnitude of the amplification factor) should be exactly one. However the above temporal treatment of the Coriolis term is not exactly energy conserving and so the amplitudes are slightly less than one. Interestingly, the amplitudes

15   using the asymmetric H are extremely similar to those using the symmetric H, implying that the scheme using the asymmetric H should be nearly energy conserving and stable. The zero frequency modes confirm the existence of steady geostrophic modes.

5 Accuracy of the TRiSK perp operator

The accuracy of the TRiSK perp operator (Eq. 7) is assessed by reconstructing the

20   solid body rotation velocity field of test case 2 of Williamson et al. (1992) from the normal components of this velocity field at each edge. The maximum errors in the reconstructed velocity in comparison to the analytic profile for each grid at each resolution are shown in Fig. 5. Resolution is measured by the total degrees of freedoms (number of cells plus number of edges). The errors saturate at quite coarse resolution and are

highest on the cubed-sphere grid. It is surprising how much more accurate the perp operator on the non-orthogonal HR grid is in comparison to the orthogonal version.

The perp operation can also be evaluated using a least-squares fit (Eq. 16) which is also shown in Fig. 5. The least squares fit is much more accurate than the TRiSK perp and converges with resolution but does not satisfy the important mimetic property that the divergence on the dual is a convex combination of the divergence of the primal. Therefore if the shallow-water equations were solved using the least squares operator, steady geostrophic modes would not be maintained. The consequence of using the inconsistent, TRiSK perp operator will be seen in Sect. 6.

6   Results of shallow water test cases

The time-steps used for each test case, each grid and each resolution are shown in Table 3. Time-steps are chosen to give similar advective and gravity wave Courant numbers for each grid. However the Courant numbers chosen are different for each test-case, as described in the sub-sections describing the test-case results below.

6.1   Solid body rotation (Williamson et al., 1992, test case 2)

Height and velocity errors after five days for the Williamson et al. (1992) solid body rotation, test case 2 are shown in Fig. 6 for the asymmetric H and in Fig. 7 for the symmetric H, both for coarse versions of the grids, each with similar numbers of total dofs.

For both the versions of the non-orthogonal correction, H, the centroidal, non-orthogonal version of the HR grid degrades accuracy a little in comparison to the orthogonal grid. The symmetric H severely degrades the accuracy on all grids in comparison to the asymmetric H but in particular, degrades the accuracy of the orthogonal grid. The symmetric non-orthogonal correction, H, is doing harm on an orthogonal grid whereas, the asymmetric non-orthogonal correction is zero on an orthogonal grid.

Using the asymmetric H, the maximum errors on the cubed-sphere and diamond grid are considerably larger than those on the HR grids due to the large errors at the corners and along the cube edges where the grid lines change direction abruptly and where the skewness is maximum. However away from the corners, the diamond grid gives
5   low errors.

The disadvantage of the asymmetric H is that it spoils the energy conservation properties of the spatial discretisation. In order to judge the extent of this problem, the normalised energy change for symmetric and asymmetric H for the simulations shown in Figs. 6 and 7 are shown in Fig. 8. Positive changes are solid and negative changes are
10   dashed. The symmetric H does indeed have better energy conservation.

The motivation for the grids of quadrilaterals is to avoid the computational modes of the hexagonal C-grid. The computational Rossby modes manifest themselves as grid-scale enstrophy. This is controlled using upwind advection of pv (CLUST is used here). Hence, the solid-body rotation test on the hexagonal grids loses total enstrophy
15   (bottom of Fig. 8). Because the cubed-sphere and diamond grids do not have the same modes, their enstrophy conservation is about an order of magnitude better. However this advantage of the quad grids is lost after 5 days when using the less accurate, symmetric H (bottom right of Fig. 8).

Convergence with resolution for the solid-body rotation test on all grids of the ℓ_2 and
20   ℓ_∞ error norms of geopotential and velocity is shown in Fig. 9. Resolution is measured by the total degrees of freedoms (number of cells plus number of edges). Time steps are chosen (see Table 3) to maintain an advective Courant number of about 0.14 and a gravity wave Courant number of about 0.7, apart from at the lowest resolutions which need a shorter time-step in order to represent the scale independent Coriolis term
25   accurately. Larger Courant numbers could have been chosen but the largest time-step cannot go much above 3600 s on the coarsest grid in order to maintain accuracy of the Coriolis term.

Convergence with resolution of all error metrics of this shallow-water test case is much better than the convergence with resolution of the perp operator alone. It seems

that having the right divergence on the dual is more important for accuracy than convergence of the perp operator. In Fig. 5, the non-orthogonal HR grid has the lowest errors of the perp operator whereas solving the shallow-water equations with the same initial wind field, the orthogonal HR grid has the lowest errors, implying that other aspects of the discretisation are controlling the errors of the shallow water model for this test case, not the perp operator.

The convergence of the $\ell_2(\phi)$ error norms using the asymmetric H are close to second-order on all the grids. Using the symmetric H, the diamond and cubed-sphere convergence is similar to using the asymmetric H but the convergence of the HR grids drops to first order using the symmetric H. Convergence of the $\ell_\infty(\phi)$ norms stalls for all grids and all Hs apart from when using the orthogonal HR grid with the asymmetric H (ie diagonal H) which gives first order convergence of $\ell_\infty(\phi)$. The $\ell_2(u)$ error metrics are second-order for all configurations and the $\ell_\infty(u)$ error metrics are between first and second order, beginning to stall at the highest resolution.

From this sub-section, we have learnt the following:

– The asymmetric H mostly gives much better accuracy than the symmetric H and does not degrade accuracy on an orthogonal grid.

– Treating the HR grid as non-orthogonal increases error a little.

– The cubed-sphere grid has higher errors at all resolutions considered and lower order of accuracy in comparison to the HR grids.

– The diamond grid has better convergence with resolution and lower errors in comparison to the cubed-sphere grid when using the asymmetric H.

– The accuracy of the solution of the shallow-water equations for this test case is not directly related to the accuracy of the perp operator.

6.2 Mid-latitude mountain (Williamson et al., 1992, test case 5)

The Williamson et al. (1992) flow over a mountain (test case 5) does not have an analytic solution and so numerical solutions are compared with results of a version of the NCAR spectral transform shallow water model (STSWM Hack and Jakob, 1992) revised by Pilar Rípodas from Deutscher Wetterdienst (personal communication, 2009) and run at T426 resolution and using a time-step of 90 s and a hyper-diffusion coefficient of $4.96 \times 10^{11} \, m^4 \, s^{-1}$. The spectral model results are interpolated from the native spectral model grid (640×1280) onto the computational points of the C-grids using the bicubic interpolation code available also from Deutscher Wetterdienst. As resolution increases, the errors for this test case become very sensitive to time-stepping errors (J. Thuburn, personal communication, 2012) due to the shock of the initialisation. Therefore small gravity wave Courant numbers are used for all grids, as shown in Table 3.

The height contours and errors in comparison to the reference solution for some mid-resolution results are shown in Fig. 10. For this test case the differences between using the symmetric and asymmetric H are tiny. Additionally, considering the different resolutions used for each grid type, the errors using each grid are very similar and the errors do not impact significantly on the total height pattern. The errors are plotted piecewise constant on every cell and so it is clear that there is no obvious grid imprinting or grid-scale noise apart from on the cubed-sphere using the asymmetric H, for which the cube edges are visible in the error fields.

The convergence with resolution for all grids of the ℓ_2 and ℓ_∞ errors of geopotential are shown in Fig. 11. The symmetric and asymmetric H results give nearly identical results and all grids show remarkably similar errors with convergence between first and second for $\ell_2(\phi)$ and first order for $\ell_\infty(\phi)$. Due to the more undulating nature of the flow, the mountain test case does not suffer due to lack of grid alignment with the flow and so the problems, particularly with the cubed-sphere grid, do not show up.

Diamond C-grid

H. Weller

Title Page

Abstract | Introduction

Conclusions | References

Tables | Figures

|◄ | ►|

◄ | ►

Back | Close

Full Screen / Esc

Printer-friendly Version

Interactive Discussion

6.3 Galewsky et al. (2004) unstable jet

The Galewsky et al. (2004) barotropically unstable jet is challenging because the instability can be released prematurely by truncation errors related to lack of grid alignment, grid inhomogeneity, or asymmetries in the discretisation. The test case is used with an initial perturbation and without viscosity. There is no analytic solution and so the results are compared with the STSWM reference model run at T426 using a time-step of 30 s and a hyper-diffusion coefficient of $4.97 \times 10^{11} \, \text{m}^4 \, \text{s}^{-1}$. The relative vorticity after 6 days for the reference solution and all of the C-grids is shown in Fig. 12. The results of the spectral model are interpolated onto HR grid 8 and the vorticity is plotted piecewise constant in exactly the same was as for the C-grid results. All of the C-grids use the asymmetric H and the results using the symmetric H are visually identical.

The unstable jet using both version of the HR grid is very similar to the reference solution except that the HR grid results have spurious vorticity stripes upstream of steep gradients caused by phase errors of the vorticity when using the energy conserving version of TRiSK. In contrast, the results using the cubed-sphere or the diamond grid contain dramatic wave number 4 patterns which are not showing any signs of lessening with increasing resolution. If this test case is indicative of models that do not work well in 3-D as weather or climate forecasting models, then the cubed-sphere or diamond grids should not be used with this low-order differencing scheme.

7 Conclusions

A new C-grid discretisation of the shallow-water equations suitable for non-orthogonal grids has been proposed which does not degrade the accuracy of TRiSK on orthogonal grids and is more accurate than the scheme of Thuburn et al. (2013) for one test case on grids with orthogonality less than about 28°. The new scheme formally loses energy conservation of the spatial discretisation but in tests, the energy conservation is very

similar to the scheme of Thuburn et al. (2013). The new scheme will extend to three dimensions and so can be used for non-orthogonal grids over orography.

It has been demonstrated that the TRiSK perp operator is inconsistent (zeroth order accurate) but that this does not prevent convergence with resolution of shallow-water test cases. The perp operator leads to fluxes on the dual grid which have divergence which is a convex combination of the divergence on the primal and so an aspect of the perpendicular velocity is exactly correct. This helps the accuracy of the shallow-water test cases.

A new, diamond grid of the sphere has been proposed which consists of quadrilaterals, is more orthogonal and nearly as uniform as the equal angle cubed sphere. It mostly out-performs the cubed sphere in the tests undertaken.

The grids of quadrilaterals do not admit the computational modes of the hexagonal C-grid and hence enstrophy is better conserved. However they do not outperform the hexagonal C-grid in any way and the hexagonal-icosahedral grid gives more accurate results in most test cases. However the lack of computational modes could be more beneficial in 3-D where the computational modes of the hexagonal C-grid could interact with, for example, the Hollingsworth instability. The grids of quadrilaterals can also be used within directly addressed codes already written to handle structured grids of quadrilaterals.

Supplementary material related to this article is available online at http://www.geosci-model-dev-discuss.net/6/6035/2013/ gmdd-6-6035-2013-supplement.zip.

References

Cotter, C. and Shipton, J.: Mixed finite elements for numerical weather prediction, J. Comput. Phys., 231, 7076–7091, 2012. 2012. 6038

Cotter, C. and Thuburn, J.: A finite element exterior calculus framework for the rotating shallow-water equations, J. Comput. Phys., in press, 2013. 6038

Danilov, S.: On utility of triangular C-grid type discretization for numerical modeling of large-scale ocean flows, Ocean Dynam., 60, 1361–1369, 2010. 6037

Fournier, A., Taylor, M., and Tribbia, J.: The Spectral Element Atmosphere Model (SEAM): high-resolution parallel computation and localized resolution of regional dynamics, Mon. Weather Rev., 132, 726–748, 2004. 6037

Galewsky, J., Scott, R., and Polvani, L.: An initial-value problem for testing numerical models of the global shallow-water equations, Tellus A, 56, 429–440, 2004. 6056, 6074

Gassmann, A.: Inspection of hexagonal and triangular C-grid discretizations of the shallow water equations, J. Comput. Phys., 230, 2706–2721, 2011. 6037

Hack, J. and Jakob, R.: Description of a Global Shallow Water Model Based on the Spectral Transform Method, Tech. Rep. NCAR/TN-343+STR, National Centre for Atmospheric Research, Boulder, Colorado, 1992. 6055

Heikes, R. and Randall, D.: Numerical integration of the shallow-water equations on a twisted icosahedral grid, Part II: a detailed description of the grid and an analysis of numerical accuracy, Mon. Weather Rev., 123, 1881–1997, 1995. 6039, 6040

Hortal, M. and Simmons, A.: Use of reduced Gaussian grids in spectral models, Mon. Weather Rev., 119, 1057–1074, 1991. 6036

OpenFOAM: The opensource CFD toolbox, The OpenCFD Foundation, available at: http://www.openfoam.org (last access: 27 November 2013), 2013. 6048, 6050

Rančić, M., Purser, R., and Mesinger, F.: A global shallow-water model using an expanded spherical cube: gnomonic versus conformal coordinates, Q. J. Roy. Meteor. Soc., 122, 959–982, 1996. 6037

Rančić, M., Zhang, H., and Savic-Jovcic, V.: Nonlinear advection schemes on the Octagonal Grid, Mon. Weather Rev., 136, 4468–4686, 2008. 6036

Ringler, T., Ju, L., and Gunzburger, M.: A multiresolution method for climate system modeling: applications of spherical centroidal Voronoi tessellations, Ocean Dynam., 58, 475–498, 2008. 6037, 6040

Ringler, T., Thuburn, J., Skamarock, W., and Klemp, J.: A unified approach to energy conservation and potential vorticity dynamics for arbitrarily-structured C-grids, J. Comput. Phys., 229, 3065–3090, 2010. 6037, 6038, 6044, 6045, 6046

Staniforth, A. and Thuburn, J.: Horizontal grids for global weather and climate prediction models: a review, Q. J. Roy. Meteor. Soc., 138, 1–26, 2012. 6037

Thuburn, J.: Numerical wave propagation on the hexagonal C-grid, J. Comput. Phys., 227, 5836–5858, 2008. 6037

Thuburn, J. and Cotter, C.: A framework for mimetic discretization of the rotating shallow-water equations on arbitrary polygonal grids, SIAM J. Sci. Comput., 34, 203–225, 2012. 6037, 6038, 6042, 6044, 6046, 6047

Thuburn, J., Ringler, T., Skamarock, W., and Klemp, J.: Numerical representation of geostrophic modes on arbitrarily structured C-grids, J. Comput. Phys., 228, 8321–8335, 2009. 6037, 6038, 6043

Thuburn, J., Cotter, C., and Dubos, T.: A mimetic, semi-implicit, forward-in-time, finite volume shallow water model: comparison of hexagonal-icosahedral and cubed sphere grids, Geosci. Model Dev. Discuss., in preparation, 2013. 6038, 6039, 6045, 6047, 6056, 6057

Wan, H., Giorgetta, M. A., Zängl, G., Restelli, M., Majewski, D., Bonaventura, L., Fröhlich, K., Reinert, D., Rípodas, P., Kornblueh, L., and Förstner, J.: The ICON-1.2 hydrostatic atmospheric dynamical core on triangular grids – Part 1: Formulation and performance of the baseline version, Geosci. Model Dev., 6, 735–763, doi:10.5194/gmd-6-735-2013, 2013. 6037

Weller, H.: Controlling the computational modes of the arbitrarily structured C-grid, Mon. Weather Rev., 140, 3220–3234, 2012. 6037, 6044, 6045

Weller, H., Weller, H. G., and Fournier, A.: Voronoi, Delaunay and block structured mesh refinement for solution of the shallow water equations on the sphere, Mon. Weather Rev., 137, 4208–4224, 2009. 6036

Weller, H., Thuburn, J., and Cotter, C.: Computational modes and grid imprinting on five quasi-uniform grids of the sphere, Mon. Weather Rev., 140, 2734–2755, 2012. 6037, 6046, 6051

White, P.: IFS documentation, Part III: dynamics and numerical procedures, Tech. Rep. CY23R4, ECMWF, available at: http://www.ecmwf.int/research/ifsdocs_old/DYNAMICS/index.html (last access: 27 November 2013), 2003. 6036

Williamson, D., Drake, J., Hack, J., Jakob, R., and Swarztrauber, P.: A standard test set for numerical approximations to the shallow water equations in spherical geometry, J. Comput. Phys., 102, 211–224, 1992. 6051, 6052, 6055, 6067, 6068, 6069, 6070, 6071, 6072, 6073

Diamond C-grid

H. Weller

Title Page

Abstract | Introduction

Conclusions | References

Tables | Figures

|◄ | ►|

◄ | ►

Back | Close

Full Screen / Esc

Printer-friendly Version

Interactive Discussion

Table 1. Properties of the different grids.

	number of		Δx mean	$\frac{\Delta x_{max}}{\Delta x_{min}}$	non-orthogonal (°)		skewness		non-centroidality	
	cells	dofs	(km)		mean	max	mean	max	mean	max
Orthogonal HR grid (Centroidality of the primal given. Dual is less centroidal.)										
3	162	642	1906	1.23	0	0	0.035	0.059	0.0096	0.020
4	642	2562	956	1.26	0	0	0.020	0.031	0.0063	0.019
5	2562	10 242	479	1.27	0	0	0.010	0.016	0.0033	0.017
6	10 242	40 962	239	1.27	0	0	0.0052	0.0087	0.0018	0.017
7	40 962	163 842	120	1.27	0	0	0.0026	0.0053	0.0010	0.017
8	163 842	655 362	60	1.28	0	0	0.0013	0.0045	0.0007	0.017
Non-orthogonal HR grid (Primal is centroidal. Centroidality of the dual given.)										
3	162	642	1905	1.18	0.29	0.88	0.035	0.094	0.067	0.13
4	642	2562	956	1.23	0.15	0.82	0.020	0.069	0.068	0.14
5	2562	10 242	479	1.25	0.099	0.79	0.011	0.047	0.067	0.13
6	10 242	40 962	239	1.26	0.063	0.86	0.0056	0.038	0.066	0.13
7	40 962	163 842	120	1.27	0.039	0.86	0.0029	0.036	0.066	0.13
8	163 842	655 362	60	1.28	0.029	0.89	0.0015	0.035	0.066	0.13
Equal-angle cubed sphere (Centroidality of the primal given. Dual is centroidal.)										
6 × 6	216	648	1554	1.57	2.81	8.83	0.025	0.19	0.037	0.061
12 × 12	864	2592	783	1.68	3.97	19.1	0.013	0.18	0.027	0.081
17 × 17	1734	5202	553	1.72	4.38	22.5	0.009	0.18	0.022	0.094
24 × 24	3456	10 368	392	1.74	4.68	24.8	0.017	0.10	0.017	0.10
32 × 32	6144	18 432	294	1.75	4.87	26.1	0.013	0.17	0.013	0.11
48 × 48	13 824	41 472	196	1.77	5.06	27.4	0.0034	0.17	0.009	0.12
72 × 72	31 104	93 312	131	1.78	5.19	28.3	0.0023	0.17	0.0063	0.12
144 × 144	124 416	373 248	65	1.79	5.31	29.2	0.0011	0.17	0.003	0.13
288 × 288	497 664	1 492 992	33	1.79	5.39	29.6	0.0006	0.17	0.002	0.13
Diamond grid (Primal is centroidal. Centroidality of the dual given.)										
6 × 6	432	1296	1102	1.55	1.03	2.93	0.011	0.16	0.01	0.03
12 × 12	1728	5184	552	1.69	1.89	5.67	0.0064	0.15	0.013	0.055
17 × 17	3468	10 404	390	1.76	2.11	7.07	0.0046	0.15	0.011	0.067
24 × 24	6912	20 736	276	1.81	2.21	7.87	0.0032	0.15	0.009	0.077
32 × 32	12 288	36 864	207	1.85	2.25	8.29	0.0024	0.15	0.007	0.084
48 × 48	27 648	82 944	138	1.89	2.26	8.64	0.0016	0.15	0.005	0.091
72 × 72	62 208	186 624	922	1.95	2.26	8.86	0.0011	0.14	0.004	0.095
144 × 144	248 832	746 496	461	2.03	2.24	9.07	0.0005	0.14	0.002	0.10

Table 2. Variables used in the discretisation and some of their finite-volume representations. Extensive quantities are upper case.

Variable	Definition	Description
Indexing		
i, j		Indexing for primal cells (dual vertices)
e, e'		Indexing for (primal and dual) edges
v, w		Indexing for primal vertices (dual cells)
Geometry		
$\boldsymbol{x}_i$, $\boldsymbol{x}_v$		Location of dual/primal vertex i, v
$\boldsymbol{x}_e$		Primal/dual edge e cross-over point
$\boldsymbol{p}_e$	$p_e \hat{\boldsymbol{p}}_e$	Surface normal vector to primal edge e
$\boldsymbol{p}_e^{\perp}$	$\boldsymbol{k} \times \boldsymbol{p}_e$	Perpendicular with same magnitude
$\boldsymbol{d}_e$	$d_e \hat{\boldsymbol{d}}_e$	Surface normal vector to dual edge e
$\boldsymbol{d}_e^{\perp}$	$\boldsymbol{k} \times \boldsymbol{d}_e$	Perpendicular with same magnitude
A_i, A_v		Area of cell i, v
A_{iv}		Overlap area between primal cell i and dual cell v
A_e		Area associated with edge e
A_{ie}		Fraction of A_e in cell i
A_{ive}		Fraction of A_{ie} in dual cell v
n_{ei}	$\text{sign}(\boldsymbol{p}_e \cdot (\boldsymbol{x}_e - \boldsymbol{x}_i))$	Edge orientation indicator
n_{ev}	$\text{sign}(\boldsymbol{d}_e \cdot (\boldsymbol{x}_e - \boldsymbol{x}_v))$	
Intensive quantities		
ϕ_i		Geopotential at $\boldsymbol{x}_i$
ϕ_e		Geopotential at $\boldsymbol{x}_e$
q_v	$\frac{f+\varsigma}{h}$	Potential vorticity at $\boldsymbol{x}_v$
q_e		Potential vorticity at $\boldsymbol{x}_e$
k_i	$\frac{1}{2A_i} \sum_{e \in \text{EC}(i)} \frac{A_{ie}}{A_e} U_e V_e$	Kinetic energy at $\boldsymbol{x}_i$
Extensive quantities		
U_e	$\boldsymbol{v}_e \cdot \boldsymbol{p}_e = HV$	Flux through primal face e
V_e	$\boldsymbol{v}_e \cdot \boldsymbol{d}_e^{\perp}$	Circulation along dual edge e

Title Page

Abstract | Introduction

Conclusions | References

Tables | Figures

◀ | ▶|

◀ | ▶

Back | Close

Full Screen / Esc

Printer-friendly Version

Interactive Discussion

Table 3. Grid resolutions and time steps used for all test cases and resulting advective Courant numbers (C_a) and gravity-wave Courant numbers (C_g).

	dofs	Test 2			Test 5			Jet		
		Δt (s)	C_a	C_g	Δt (s)	C_a	C_g	Δt (s)	C_a	C_g
HR grid										
3	642	3600	0.07	0.36						
4	2562	3600	0.14	0.72	1800	0.04	0.5			
5	10 242	1800	0.14	0.72	900	0.04	0.5			
6	40 962	900	0.14	0.72	450	0.04	0.5			
7	163 842	450	0.14	0.72	225	0.04	0.5	600	0.4	1.8
8	655 362	225	0.14	0.72				300	0.4	1.8
Equal-angle cubed-sphere										
6 × 6	648	3600	0.11	0.50						
12 × 12	2592	3600	0.22	1.0	1200	0.04	0.5			
17 × 17	5202	2400	0.21	1.0	900	0.04	0.6			
24 × 24	10 368	1800	0.23	1.1	600	0.04	0.5			
32 × 32	18 432	1200	0.20	1.0						
48 × 48	41 472	900	0.22	1.1	300	0.04	0.6			
72 × 72	93 312	600	0.23	1.1	225	0.04	0.6	400	0.3	1.5
144 × 144	373 248	300	0.23	1.1	100	0.04	0.6	200	0.3	1.5
288 × 288	1 492 992	150	0.23	1.1				100	0.3	1.5
Diamond grid										
6 × 6	1296	3600	0.14	0.7						
12 × 12	5184	2400	0.20	1.0	900	0.04	0.6			
17 × 17	10 404	1800	0.23	1.1	600	0.04	0.6			
24 × 24	20 736	1200	0.22	1.1	450	0.04	0.6			
32 × 32	36 864	900	0.22	1.1						
48 × 48	82 944	600	0.23	1.1	225	0.04	0.7			
72 × 72	186 624	450	0.26	1.3	150	0.04	0.7	240	0.2	1.4
144 × 144	746 496	225	0.26	1.4				120	0.2	1.5
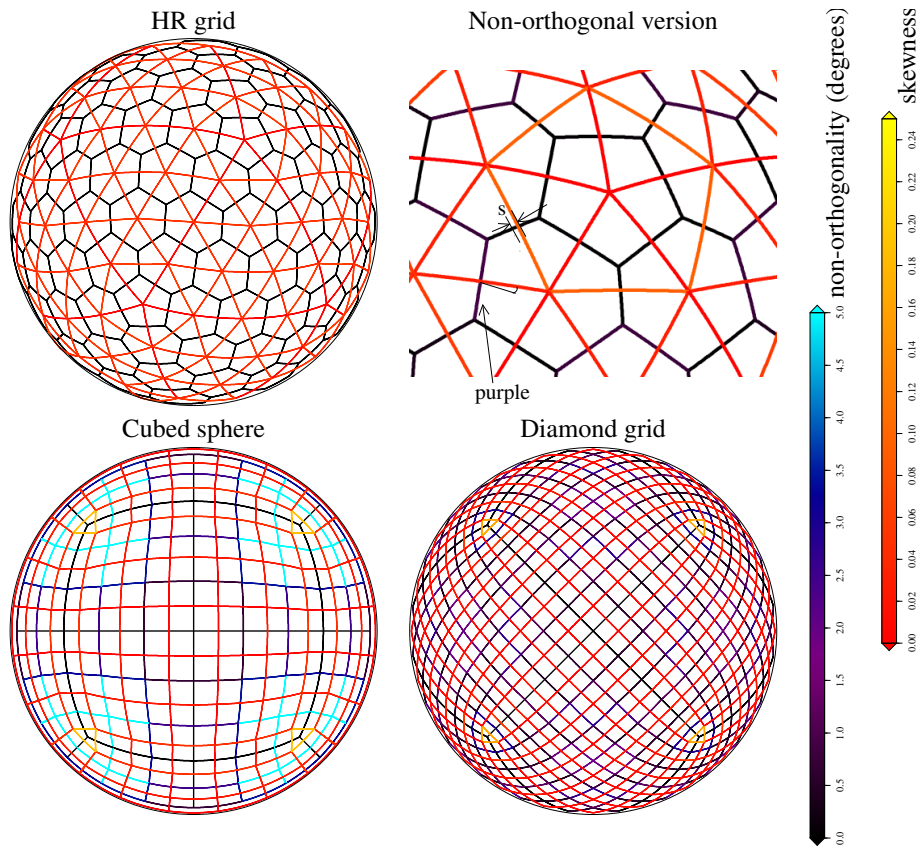
Fig. 1. Orthogonality and skewness of grid types. Non-orthogonality (from black, orthogonal, to blue) is shown on the primal edges whereas skewness or the primal grid (from red, no skewness, to yellow) is shown on the dual edges. The "s" in the non-orthogonal HR grid shows the skewness (the normlised difference between the primal edge mid-point and the edge cross-over point).
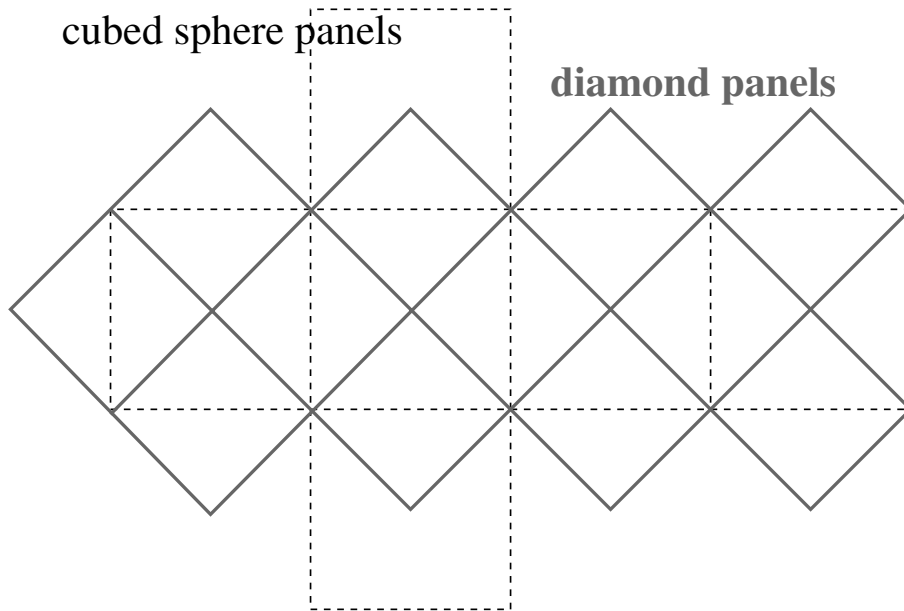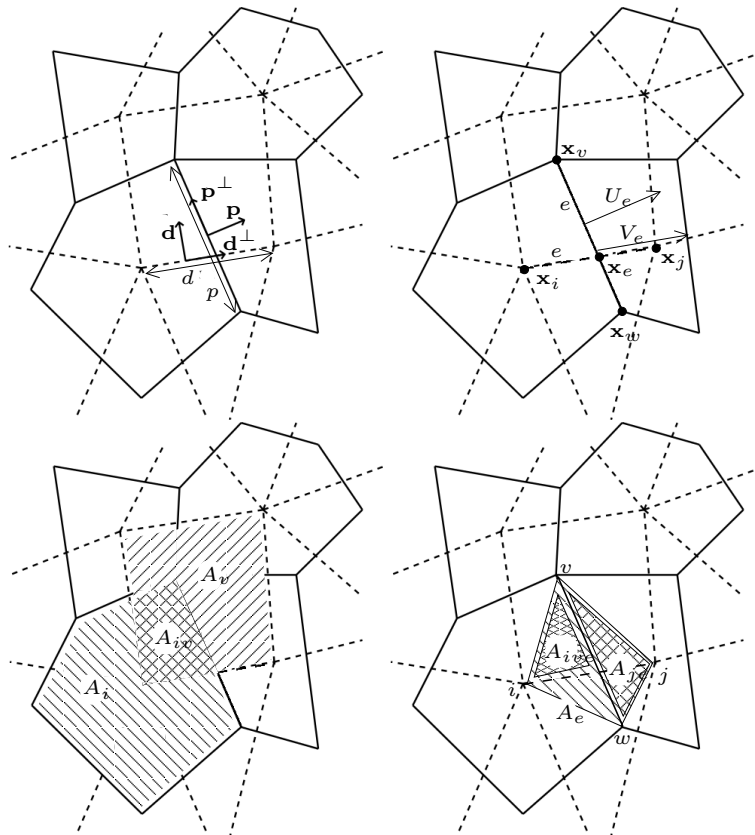
cubed sphere panels

diamond panels

Fig. 2. The panels of the cubed sphere primal grid (dashed) and the diamond primal grid (grey).

Title Page

Abstract | Introduction

Conclusions | References

Tables | Figures

|◄ | ►|

◄ | ►

Back | Close

Full Screen / Esc

Fig. 3. Primal grid (solid) and dual grid (dashed) with surface normal vectors, $\boldsymbol{p}$ and $\boldsymbol{d}$, perpendicular vectors $\boldsymbol{p}^\perp$ and $\boldsymbol{d}^\perp$, lengths $p = |\boldsymbol{p}| = |\boldsymbol{p}^\perp|$ and $d = |\boldsymbol{d}| = |\boldsymbol{d}^\perp|$, flux $U_e = \boldsymbol{v} \cdot \boldsymbol{p}$ and circulation $V_e = \boldsymbol{v} \cdot \boldsymbol{d}^\perp$, for edge e of the primal or dual.

Title Page

Abstract | Introduction

Conclusions | References

Tables | Figures

|◀ | ▶|

◀ | ▶

Back | Close

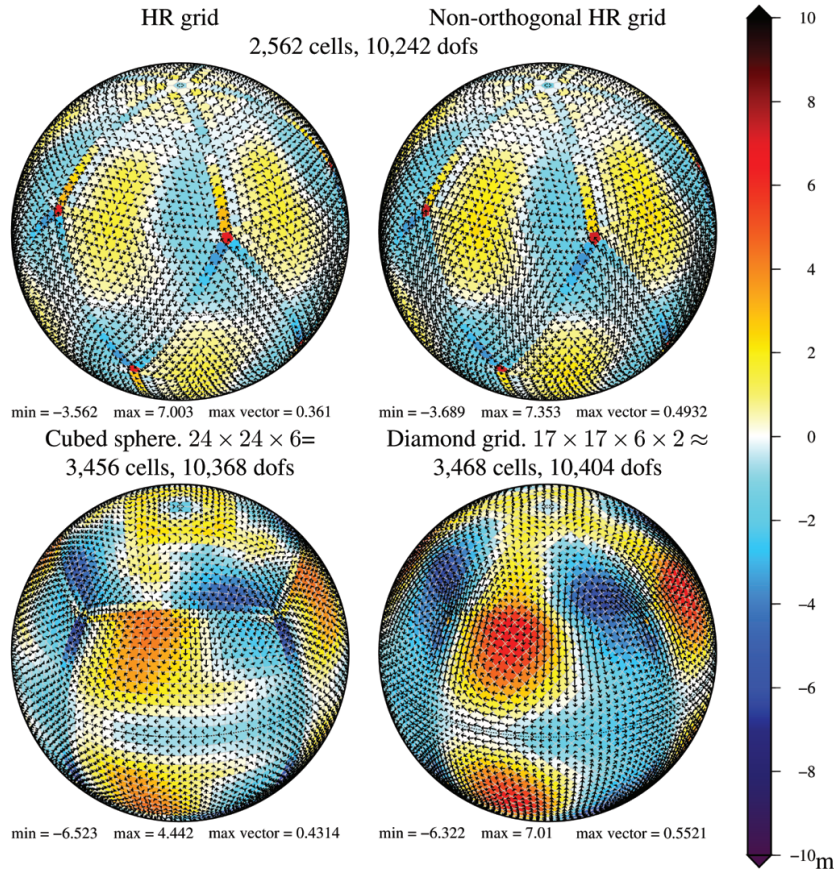Full Screen / Esc

Printer-friendly Version

Interactive Discussion
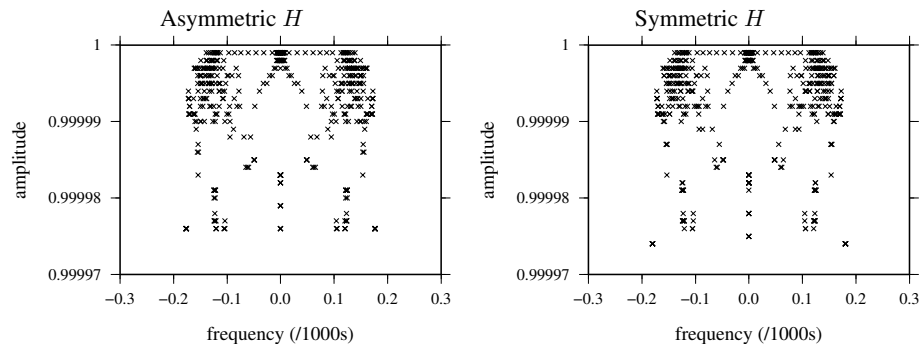
Fig. 4. Amplitudes and frequencies of the normal modes of the linearised shallow water equations discretised on a cubed sphere grid of 648 dofs using the non-orthogonal schemes with both the symmetric and asymmetric versions of the non-orthogonal correction, *H*.
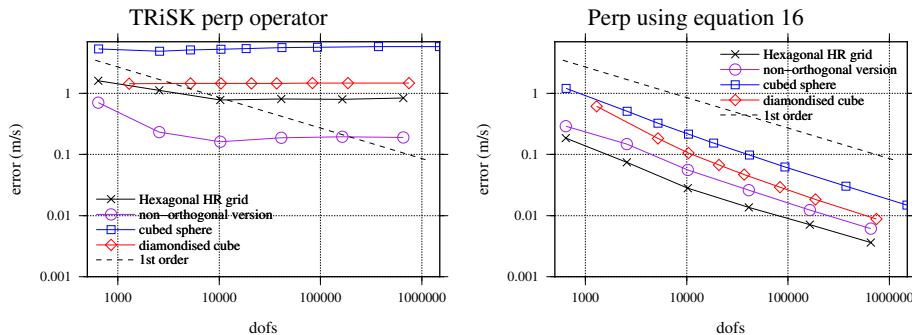
Fig. 5. Maximum errors in the velocity tangential to each edge reconstructed from the normal components of the solid body rotation velocity field from test case 2 of Williamson et al. (1992). These errors can be compared with the maximum velocity of $38\,\mathrm{m\,s^{-1}}$.

Full Screen / Esc

Printer-friendly Version

Interactive Discussion
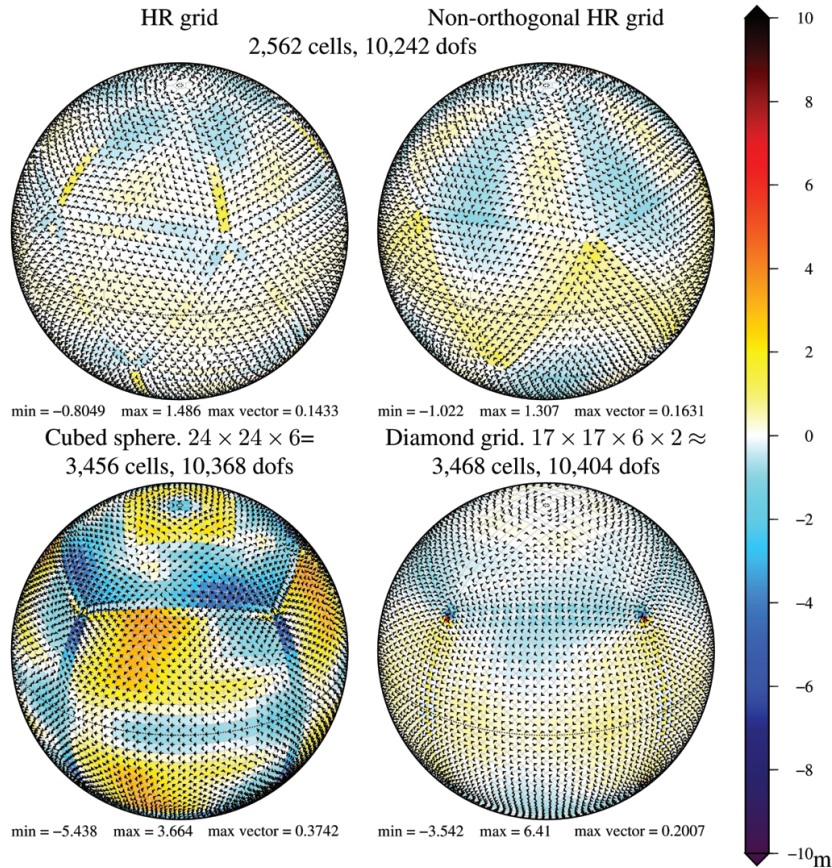
Fig. 6. Height and velocity errors for Williamson et al. (1992) test case 2 after 5 days. Asymmetric H. Time-step of 1800 s.

Title Page

Abstract | Introduction

Conclusions | References

Tables | Figures

|◄ | ►|

◄ | ►

Back | Close

Full Screen / Esc

Printer-friendly Version

Interactive Discussion

Fig. 7. Height and velocity errors for Williamson et al. (1992) test case 2 after 5 days. Symmetric H. Time-step of 1800 s.
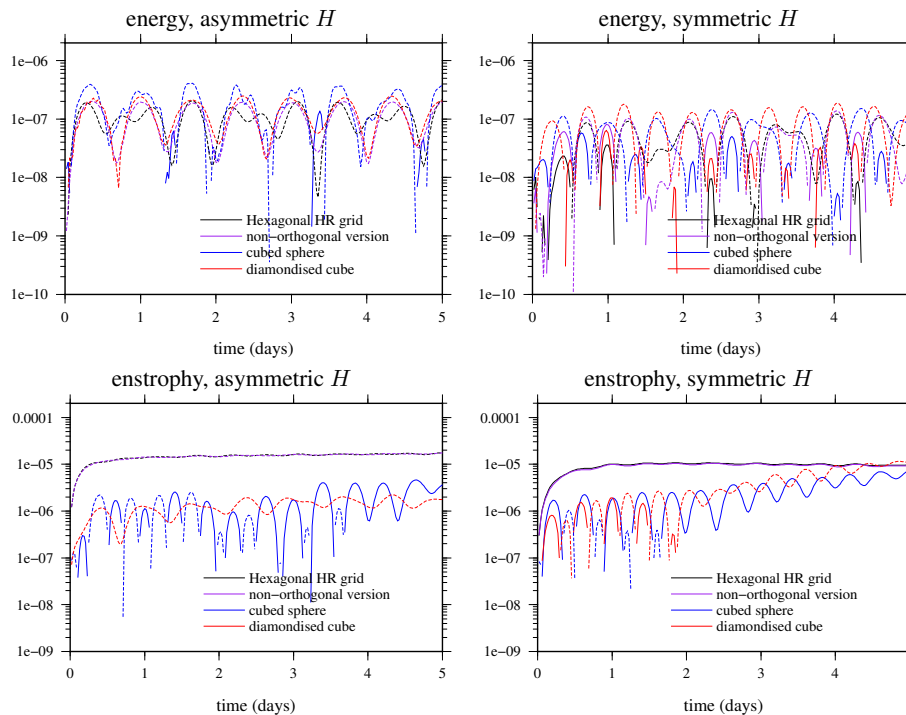
Fig. 8. Time series of normalised energy and enstrophy change for Williamson et al. (1992) test case 2. Same simulations as Figs. 6 and 7. Dashed lines show negative normalised energy and enstrophy change.
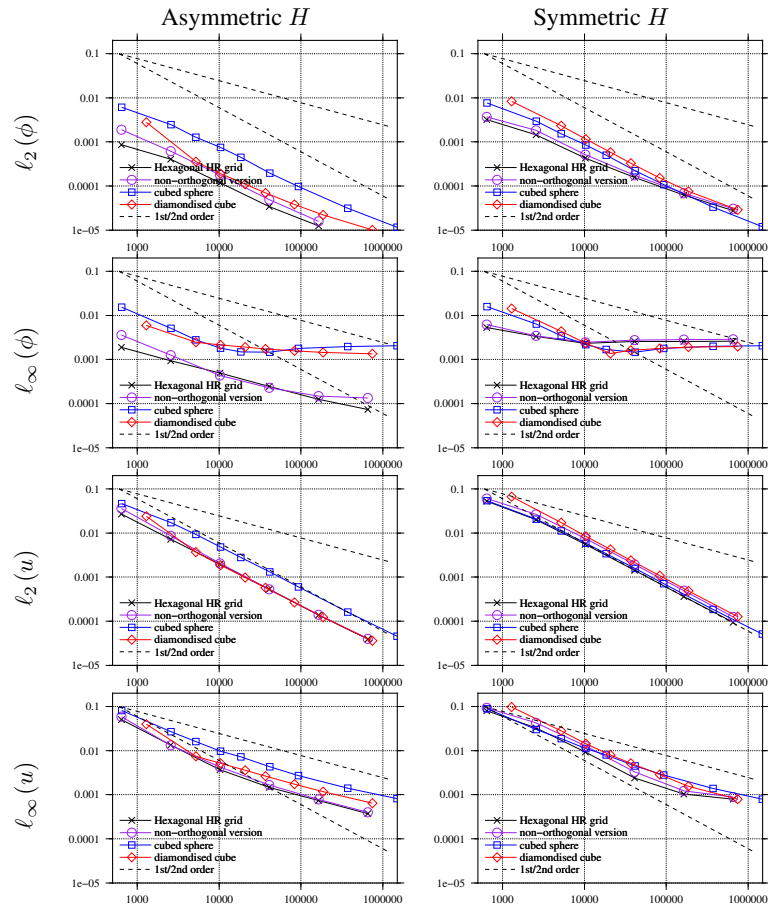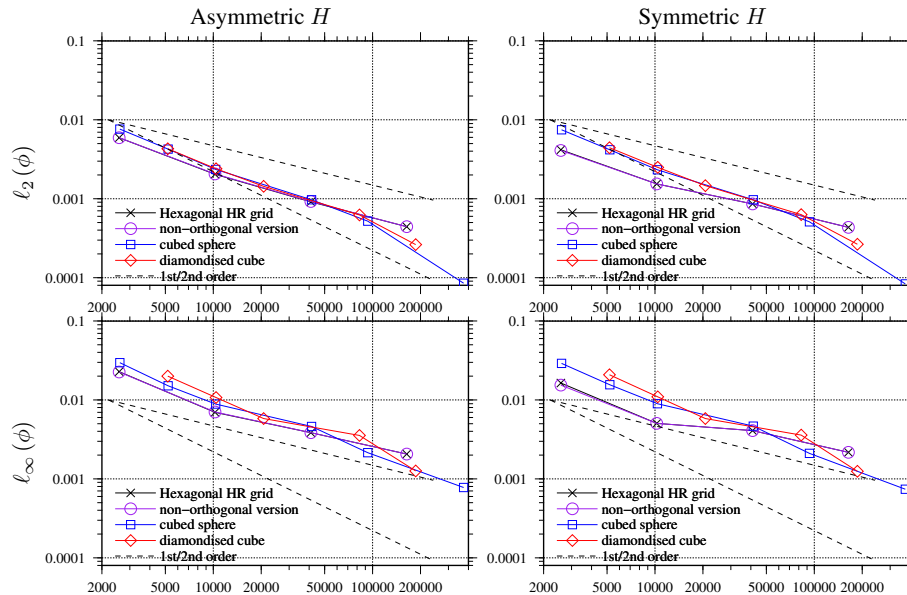
Fig. 9. Convergence of error metrics with resolution for Williamson et al. (1992) test case 2 after 5 days.

Title Page

Abstract | Introduction

Conclusions | References

Tables | Figures

|◄ | ►|

◄ | ►

Back | Close

Full Screen / Esc

Printer-friendly Version

Interactive Discussion
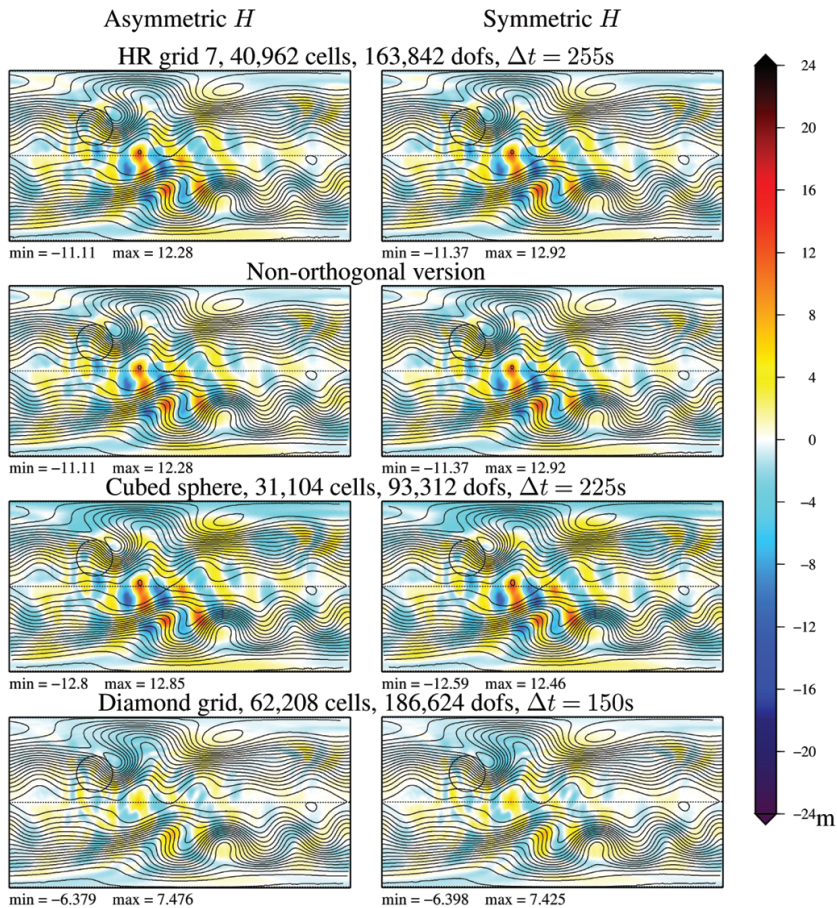
Fig. 10. Height errors (coloured) and total height (contours every 50 m) for Williamson et al. (1992) test case 5 after 15 days.

Title Page

Abstract | Introduction

Conclusions | References

Tables | Figures

◀ | ▶|

◀ | ▶

Back | Close

Full Screen / Esc

Printer-friendly Version

Interactive Discussion

Fig. 11. Convergence of error metrics with resolution for Williamson et al. (1992) test case 5 after 15 days.
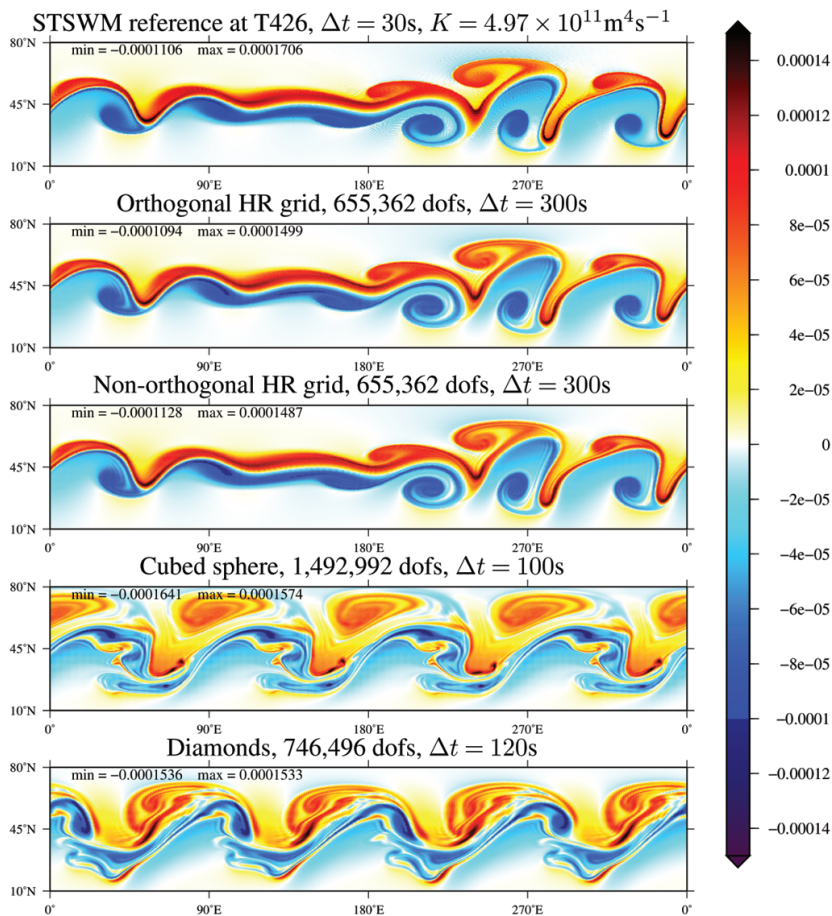
Fig. 12. Vorticity after 6 days for the Galewsky et al. (2004) unstable jet. Asymmetric H.